PHILOSOPHICAL TRANSACTIONS A

rsta.royalsocietypublishing.org

Research

Cite this article: Jaksic V, O'Shea R, Cahill P, Murphy J, Mandic DP, Pakrashi V. 2015 Dynamic response signatures of a scaled model platform for floating wind turbines in an ocean wave basin. *Phil. Trans. R. Soc. A* **373**: 20140078. http://dx.doi.org/10.1098/rsta.2014.0078

One contribution of 17 to a theme issue 'New perspectives in offshore wind energy'.

Subject Areas:
ocean engineering, structural engineering

Keywords:
offshore wind energy, tension-leg platform, structural dynamics, delay vector variance, signal nonlinearity

Author for correspondence:
V. Pakrashi
e-mail: v.pakrashi@ucc.ie

Electronic supplementary material is available at http://dx.doi.org/10.1098/rsta.2014.0078 or via http://rsta.royalsocietypublishing.org.

THE ROYAL SOCIETY PUBLISHING

Dynamic response signatures of a scaled model platform for floating wind turbines in an ocean wave basin

V. Jaksic[1,3], R. O'Shea[2,3], P. Cahill[3], J. Murphy[1], D. P. Mandic[4] and V. Pakrashi[3]

[1]Hydraulics and Maritime Research Centre (HMRC), School of Engineering, University College Cork, Youngline Industrial Estate, Pouladuff Road, Cork, Ireland
[2]Energy Engineering, School of Engineering, and [3]Dynamical Systems and Risk Laboratory, Civil and Environmental Engineering, School of Engineering, University College Cork, College Road, Cork, Ireland
[4]Department of Electrical and Electronic Engineering, Imperial College London, London SW7 2BT, UK

Understanding of dynamic behaviour of offshore wind floating substructures is extremely important in relation to design, operation, maintenance and management of floating wind farms. This paper presents assessment of nonlinear signatures of dynamic responses of a scaled tension-leg platform (TLP) in a wave tank exposed to different regular wave conditions and sea states characterized by the Bretschneider, the Pierson–Moskowitz and the JONSWAP spectra. Dynamic responses of the TLP were monitored at different locations using load cells, a camera-based motion recognition system and a laser Doppler vibrometer. The analysis of variability of the TLP responses and statistical quantification of their linearity or nonlinearity, as non-destructive means of structural monitoring from the output-only condition, remains a challenging problem. In this study, the delay vector variance (DVV) method is used to statistically study the degree of nonlinearity of measured response signals from a TLP. DVV is observed to create a marker estimating the degree to which a change in signal nonlinearity reflects real-time behaviour of the structure and also to establish the sensitivity of the instruments employed to these

changes. The findings can be helpful in establishing monitoring strategies and control strategies for undesirable levels or types of dynamic response and can help to better estimate changes in system characteristics over the life cycle of the structure.

1. Introduction

Offshore renewable energy solutions, with technological advancements and mapping of global wind resource, have the potential to be an important part of energy production worldwide. Europe has an ambition to generate 460 GW from offshore wind and 188 GW from ocean energy by the year 2050, while the international targets in offshore wind and ocean energy are 1150 GW and 748 GW, respectively [1].

Current commercial offshore substructures are economically limited to a maximum water depth of 50 m [2]. In order to capitalize on high-speed and high-quality winds over deep waters, the idea of floating platforms for offshore wind turbines has been developed [3]. Floating platforms are considered to be cost-competitive as compared with fixed-based foundations because construction in depths over 50 m does not require significant building material [2,4]. Moreover, reduced geotechnical requirements of floating wind foundations mean that core sampling is only needed to test the seabed ahead of appropriate anchor selection, as opposed to the necessity of core sampling at every pile site [3]. Also, floating turbine platforms are designed to be assembled in port and towed into position using simple barges or tugboats. This can result in major cost savings and greatly increased flexibility in construction. Generally, in comparison with fixed foundation turbines, floating wind turbines have lower installation costs [5]. The floating nature of the structure reduces site design dependency and work at sea. Land-based labour is maximized, quayside assembly and float-out strategies are integrated, and system weight, anchoring and mooring costs are reduced. Maintenance and removal costs are also reduced [5]. Finally, floating turbines address environmental concerns related to visual and noise pollution by allowing wind farms to be pushed further offshore and out of sight. Sea-life disturbance can also be minimized with elimination of foundations, reducing negative environmental impacts.

Different designs are being actively tested off the coast of Denmark, France, Germany, the Netherlands, Norway, Portugal, Spain, Sweden and the UK [6,7]. Out of 40 deep-water wind projects, more than 60% are located in Europe [3]. These prototypes are still at an early stage, far from mass production and commercialization, but are gaining attention. Presently, four full-scale offshore wind turbines on floating substructures are operating, one in the North Sea, one in the Atlantic [2] and two in the Pacific [8]. It is reported that, in addition to the four full-scale deep offshore turbines, there are three grid-connected experimental floating substructures and 35 deep-water designs under development worldwide [3,8]. The INWORK report presents the global floating offshore wind foundation development in the USA, Europe and Japan [8]. According to this report, five full-scale floating offshore turbines are planned to be installed in 2014, two in 2014/2015 and three in 2015, worldwide. Despite the fact that a number of these solutions are available in concept [8–10], a complete understanding of the behaviour of floating platforms is not present and still demands significant investigation [11]. These offshore structures have widely variable and complex dynamic responses due to intense and complex environmental loading dominated by high wind and wave forces at the locations of their operation [12–15]. Monitoring of this complex dynamics is important for offshore wind energy solutions because the exposure to wind, wave and combined wind–wave loading can be widely variable [16–19] and may lead to significant practical issues for successful implementation of this technology at its site [20,21]. Additionally, when deployed offshore, a wind turbine may also pose problems related to operations and maintenance [22,23] due to significant lack of access after installation. Therefore, quantitative estimates based on the dynamic responses and assessments of markers related to such dynamics at an early stage of development are only possible through appropriate simulation and scaled testing in laboratory conditions [21].

The detection, characterization and estimation of dynamic properties of offshore wind structures can minimize costs related to operations and maintenance, minimize risk to the system through continuous monitoring, develop early warning systems for potential failures and lead to the development of control systems to suppress undesirable dynamics [24]. Development of control systems for remote monitoring of dynamics of these energy devices has significant economic implications [25] as excessive dynamic response can lead to a forced downtime of power generation. Measurements of dynamic responses of a scaled floating foundation model in a wave tank are essential for the understanding and assessment of their dynamic responses, as experimentation in sea can often be difficult and expensive at the design stage. The quantification of linearity or nonlinearity of the dynamic response signals as indicators of the nature of the structure and changes within is an important problem which has not yet received significant attention. In other fields, this has been investigated through time-series methods, employing the outputs of system responses and then attempting to relate a marker of the response to the nonlinearity in the system [26–28].

There are many methods for characterizing a time-series signal. In this regard, a well-known technique for detecting the nature or nonlinearity of time series is the surrogate data method [29] based on statistical hypothesis testing, which presents an indirect way of detecting signal nonlinearity [30,31]. Many nonparametric analysis techniques have been developed for the detection of nonlinearity in a signal [32,33]. Using the surrogate data methodology Mandic & Chambers [34] introduced the delay vector variance (DVV) method for detecting determinism and nonlinearity in a time series. The DVV method characterizes a time series based on its predictability and compares the results with those obtained for linearized versions of the signal, i.e. surrogate data. The DVV method is further elaborated and tested in Gautama *et al*. [33,35,36] and Mandic *et al*. [37]. They show that this characterization, although not requiring any prior knowledge about the signal, is robust to the presence of noise, straightforward to interpret and visualize nonlinearity and typically exhibits improved performance over other available methods. Also, they show that the DVV method can be used for estimating the degree of signal nonlinearity by calculating the root mean squared error (RMSE) [33]. The DVV method has been successfully applied in the past to analyse the nature of biomedical signals, such as hand tremor, electroencephalogram (EEG) signals [36], functional magnetic resonance imaging [33,38], electrocardiograms, heart rate variability [38,39], and in finance [40]. Application of the DVV method in diagnostic medicine shows that the linear or nonlinear nature of the signal conveys information concerning the health condition of the subject [38,41,42]. Andrzejak *et al*. [43] analyse dynamical brain properties and find the strongest indication of nonlinear deterministic dynamics for epileptic seizures, and no significant indication of nonlinearity for healthy subjects. Gautama *et al*. [36] show that DVV analysis enables a comprehensive characterization of the dynamical modes of EEG signals, allowing for accurate classification of the brain states. The method of Gautama *et al*. [33] indicates that a difference in signal nonlinearity may also be attributed to a difference in system nonlinearity. Hongying & Fuliang [44] apply the DVV method for analysing diesel engine vibration under different conditions and observe that the vibration signals of a diesel engine have strong signal nonlinearity which gets stronger as a fault in the engine becomes worse. Furthermore, they use the root mean square (RMS) deviation of the DVV scatter diagram from its bisector line as a quantitative marker of the fault state and conclude that the method could be used to detect faults in diesel engines and other equipment by relating the fault severity to the magnitude of the computed RMS deviation values. While there exists a debate in relation to what extent signal and system nonlinearities are related, the usefulness of DVV as a statistical marker to study the nature of dynamic responses of a system from the output-only condition is well established.

In this study, the DVV method is used to quantify the extent of nonlinearity of the structural system response of a model tension-leg platform (TLP) to a variable sea state. The DVV method detects the presence of determinism and nonlinearity in a time series and is based upon the examination of local predictability of a signal [34–36]; an advantage of this method lies in

employing output-only signals from the system without completely knowing the system or the input. Nonlinearities of the structural responses are estimated and compared for variability of loading for different monitoring devices and the extent to which such nonlinearity estimates can be interpreted and used.

Dynamic responses of a Froude-scaled TLP wind turbine support structure in a wave tank are considered. The experimental arrangement corresponds to a full-scale 50 m water depth, which is in the range of minimum water depth required for this type of floater to become cost-competitive [2,10,45]. Sclavounos *et al*. [46] compared TLP and taut leg buoy concepts supporting 3–5 MW wind turbines and, among the other conclusions, found that the TLP is the preferred floater in water depths greater than 50 m [46]. Also, to evaluate the economics of floating designs, the European Wind Energy Association (EWEA) performed a comparison with jacket foundations, whose technical characteristics allow for installation in water depths of up to 45–50 m. The findings show that floating offshore wind designs are competitive in terms of levelized cost of energy with existing jacket foundations from around 50 m water depths [2]. However, Lefebvre & Collu [47] state that it becomes increasingly difficult to obtain high tension in tendons with increasing depth and therefore TLPs are limited to shallower water. Also, an INWORK report [8] presents the list of global floating offshore wind foundation development worldwide where minimum required water depths for TLPs are 25 m (GICON—German Baltic Sea; full scale planned for 2014); 50 m (Blue H TLP—the Netherlands; full scale planned for 2014); 65 m (Pelastar TLP—UK; full scale by 2015 if founded) and 60 m (Mitsui TLP—Japan and Ocean Breeze—UK; design stage).

In this study, the dynamic responses of the TLP have been monitored at different locations using load cells, a camera-based motion recognition system and a laser Doppler vibrometer (LDV). The dynamic responses of the structure have been observed for various frequencies of regular wave conditions and sea states characterized by the Bretschneider, the Pierson–Moskowitz and the Joint North Sea Wave Observation Project (JONSWAP) spectra. The degree of linearity of recorded responses has been calculated using the DVV method in order to benchmark behaviour of the structure and to compare the performance of the monitoring devices due to the changing wave characteristics. The study forms a basis for encouraging further studies in estimating markers of nonlinearities in relation to responses of offshore wind turbines.

2. Experimentation

(a) Tension-leg platform model

The TLP tested in this study is a truss-type structure with a hexagonal base fabricated from PVC piping. The scale of the model is 1 : 50. The model is scaled following Froude scaling laws, which are commonly used for scaling for offshore structures [48,49]. The floating hexagonal platform of the TLP is connected with six mooring tethers (ties), one at each corner of the platform, to the large circular anchoring gravity base which sits on the bottom of the wave basin during testing. The floating hexagonal platform consists of two main sections, the buoyancy ring and the upper structure. The buoyancy ring consists of six 90 mm diameter PVC pipes joined to the central column by six 40 mm outer diameter PVC pipes. The 500 mm tall central column is fabricated from 160 mm diameter PVC pipe and provides sufficient buoyancy to counteract the weight of the tower and nacelle. Situated 330 mm above the buoyancy ring is the upper structure, fabricated from 40 mm outer diameter PVC pipe which is joined to the buoyancy ring by six 40 mm diameter sections of pipe and to the central column by six 40 mm outer diameter PVC pipes. The upper structure provides no buoyancy as it is not submerged. The excess buoyancy force is imparted on the six 2 mm diameter stainless steel wires used as the mooring lines to ensure that they remain in tension at all times. They are connected to a stainless steel rigging-screw which allows easy adjustment of the mooring line tension when the model is in the basin. The mooring line tension has a tendency to drift from the initial pre-tension induced on the lines during wave tests at smaller model scales, therefore a method of adjustment is compulsory. The wind turbine

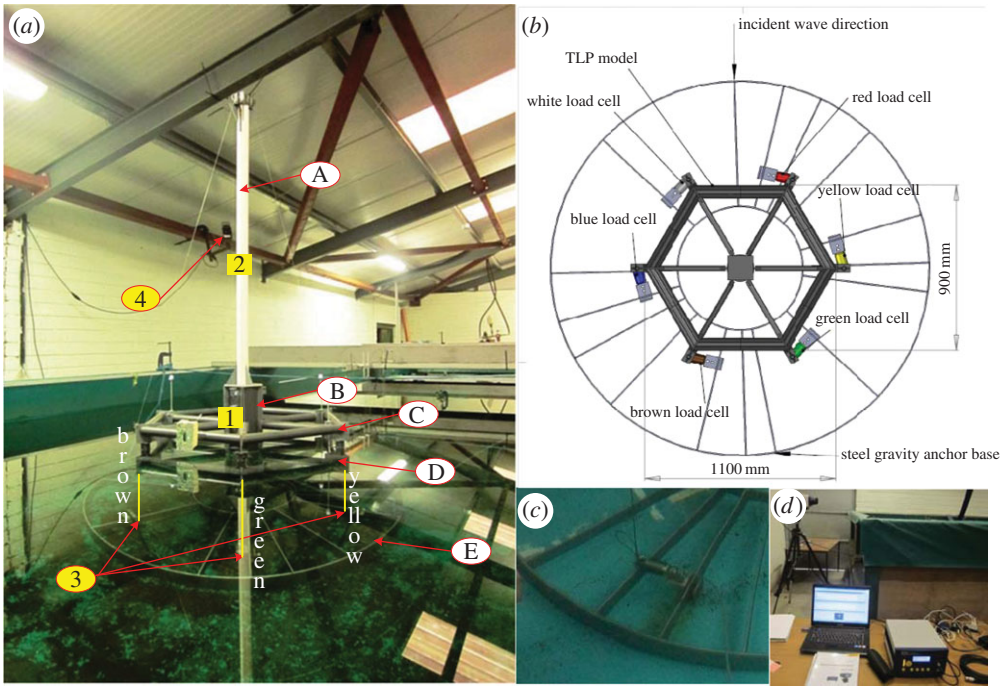

Figure 1. (*a*) 1 : 50 scale model of a truss-type TLP experimental set-up: (A) mast, (B) central column, (C) upper structure, (D) buoyancy ring and (E) gravity anchoring base. Locations of monitoring: (1) and (2) LDV focus points, (3) motion camera, and (4) load cells; (*b*) TLP gravity base with load cell arrangement; (*c*) load cell attached to anchor; and (*d*) LDV equipment. (Online version in colour.)

Table 1. Table of model specification.

element	unit	value	element	unit	value
rotor and nacelle	kg	2.2	moment of inertia (I_{xx}, I_{yy})	kg m^2	2.26
tower	kg	0.8	moment of inertia (I_{zz})	kg m^2	0.26
tower stiffness	N m^{-1}	411.9	radius of gyration (k_{xx}, k_{yy})	m	0.35
tower-bending frequency	Hz	185.5	radius of gyration (k_{zz})	m	0.15
platform	kg	16.8	displacement volume	m^3	0.0299
draft	mm	240	total weight	N	186.4
maximum *X*	mm	1100	total buoyancy	N	258.4
maximum *Y*	mm	900	total tie load	N	72
			individual tie	N	12

tower (mast) is a 1.15 m high 50 mm diameter PVC pipe with the scaled rotor and nacelle weight attached at the top. The experimental set-ups of the TLP, gravity base with load cell arrangement, load cell location and LDV equipment are shown in Figure 1*a–d*, respectively. Table 1 summarizes the specifications of the TLP model tested.

(b) Instrumentation

Behaviour of the TLP system exposed to waves of known characteristics for a period of time was recorded in a laboratory environment. Measurements required for effective analysis of the

TLP performance include the instantaneous motions of the platform, the loading on the platform mooring system and the incident wave field. The following sensors and probes were used during the testing of the device: LDV, six load cells, two water-level probes and four motion capture cameras.

The dynamic response of the TLP structure was measured using a polytec RSV-150 remote sensing vibrometer (figure 1*d*). The LDV is still a relatively new measurement tool but it allows for rapid, accurate, non-contact and long-distance measurement of vibrating structures [50–52]. The LDV was monitoring displacement and velocity of the TLP in the incident wave direction at a frequency of 600 Hz. There were two targeting points: (i) the base of the central column B and (ii) the midpoint of the mast A (figure 1*a*).

Six load cells were attached to a steel base at the bottom of the wave basin (figure 1*c*). The positions of the load cells are indicated in figure 1*a*. The Tedea–Huntleigh stainless steel single-ended bending beam load cells with a maximum load of approximately 50 N load measured the tension in each of the six mooring lines at 32 Hz and were bolted to the gravity base. Each load cell was given a colour code (name) during the testing. The load cells with names white, red, blue, yellow, brown and green are located at bow port, bow starboard, amidships port, amidships starboard, stern port and stern starboard, respectively (figure 1*b*).

Two water-level probes were situated on either side of the model. These probes measured the height of the water in millimetres during testing and could therefore measure the profile of the waves generated in the wave basin which the model was exposed to. The positions of the probes remained constant for all tests.

In order to measure the motions of the TLP during testing, four reflective markers were attached to the four corners of the hexagonal base, which allowed for redundancy in the event of splashing. The instantaneous positions were monitored by four Qualisys 3-Series Oqus marker-tracking cameras with a sampling frequency of 32 Hz (one of which is seen in figure 1). The load cells and wave probes were triggered by National Instruments LabVIEW 2011 V. 11.0 software. The Qualisys marker-tracking system was time synchronized with LabVIEW.

(c) Experimental procedure

The model testing was carried out in the ocean wave basin at the Hydraulics and Maritime Research Centre (HMRC), University College Cork (UCC), Ireland. The wave basin is 25 m long, 18 m wide and 1 m deep and the TLP was placed centrally in this. The tank has 40 flap-type paddles capable of generating sinusoidal wave profiles as well as two-dimensional and three-dimensional wave spectra. The water depth is constant at 1.0 m and corresponds to conditions within 50 m depth of sea and the scope of the interpretation of this study is limited by this depth. The device was tested for a range of wave periods, wave heights and wave spectra. Prior to testing each set-up/configuration, a stillwater measurement was recorded, which allows the deviation of the platform positions and mooring loads from the hydrostatic condition to be calculated for each hydrodynamic test. The TLP was tethered to the gravity base using six mooring lines with a mass attached to the top of the mast to simulate the weight of a wind turbine nacelle. The TLP was exposed to scaled wave heights of 40 mm, 60 mm, 90 mm and 120 mm of varying wave periods corresponding to 1 m, 3 m, 4.5 m and 6 m prototype wave heights, respectively, as well as two-dimensional Bretschneider, Pierson–Moskowitz and JONSWAP wave spectra. The sine waves were checked for steepness and they proved to be stable (e.g. not breaking), i.e. wave height over wavelength is less than 1/7. The wavelength L is calculated [53] as

$$L = 1.56 \times T^2, \tag{2.1}$$

where T is the wave period.

The effects of reflected waves at the boundaries of the basin were removed by dissipating the energy in an immersed barrier made of randomly oriented, rigid objects. The test schedule is shown in table 2.

Table 2. TLP test schedule.

Tedea–Huntleigh load cells			LDV		
input type	wave height (mm)	wave period (s)	input type	wave height (mm)	wave period (s)
monochromatic	40	1.84; 1.98; 2.12; 2.26; 2.4; 2.55; 2.69; 2.83; 2.97; 3.11; 3.25	monochromatic	40	1.84; 1.98; 2.12; 2.26; 2.4; 2.55; 2.69; 2.83; 2.97
monochromatic	60	0.8; 1.0; 1.13; 1.27; 1.41; 1.56; 1.59; 1.63; 1.66; 1.7; 1.73; 1.77; 1.8; 1.84; 1.98; 2.12; 2.26; 2.42; 2.55; 2.69; 2.83; 2.97	monochromatic	60	0.71; 0.85; 0.99; 1.13; 1.27; 1.41; 1.56; 1.59; 1.63; 1.66; 1.7; 1.73; 1.77; 1.8; 1.84; 1.98; 2.12; 2.26; 2.40; 2.55; 2.69; 2.83; 2.97
monochromatic	90	0.71; 0.85; 1.0; 1.13; 1.27; 1.41; 1.56; 1.7; 1.84; 1.98; 2.12; 2.26; 2.4	monochromatic	90	0.71; 0.85; 0.99; 1.13; 1.27; 1.41; 1.56; 1.7; 1.84; 1.98; 2.12; 2.26; 2.4
monochromatic	120	0.85; 1.0; 1.13; 1.27; 1.41; 1.56; 1.7; 1.84; 1.98	Bretschneider	60	1.08; 1.52; 2.03; 2.50; 2.72
			Pierson–Moskowitz	60	1.08; 1.52; 2.03; 2.50; 2.72
			JONSWAP	60	1.08; 1.52; 2.03; 2.50; 2.72

3. Methodology of analysis

(a) Delay vector variance method

The DVV method [35] uses predictability of a signal in phase space to examine the determinism and nonlinearity within the signal. The method is based on time delay embedding representation of a time series $x(n)$, $n = 1, 2, \ldots, N$. The DVV method, for a given embedding parameter m, can be summarized [35,36,38,54], as follows:

1. The mean, μ_d, and standard deviation, σ_d, are calculated over all pairwise Euclidian distances between delay vectors (DVs)

$$d(i, j) = ||x(\mathrm{i}) - x(j)||, \ (i \neq j). \tag{3.1}$$

2. The sets of 'neighbouring' delay vectors $\Omega_k(r_d)$ are generated by grouping those DVs that are within a certain Euclidean distance to $x(k)$ so that

$$\Omega_k(r_d) = \{x(i) | x(k) - x(i) \leq r_d\}, \tag{3.2}$$

i.e. sets that consist of all DVs that lie closer to $x(k)$ than the certain distance

$$r_{\mathrm{d}}(n) = \mu_{\mathrm{d}} - n_{\mathrm{d}}\sigma_{\mathrm{d}} + (n-1)\frac{2n_{\mathrm{d}}\sigma_{\mathrm{d}}}{N_{\mathrm{tv}}-1}; \quad n = 1, \ldots, N_{\mathrm{tv}}. \tag{3.3}$$

In other words, taken from the interval $[\max\{0, \mu_d - n_d\sigma_d\}; \mu_d + n_d\sigma_d]$, uniformly spaced, where n_{d} is a parameter controlling the span over which to perform the DVV analysis, usually set to be 2 or 3, and N_{tv}, the number of target variance, indicates how finely the standardized distance is uniformly spaced.

3. For every set $\Omega_k(r_{\mathrm{d}})$, the variance of corresponding targets, $\sigma_k^2(r_{\mathrm{d}})$, is computed. The average over all sets $\Omega_k(r_{\mathrm{d}})$ normalized by the variance of the time series, σ_x^2, yields the measure of unpredictability, 'target variance', $\sigma^{*2}(r_{\mathrm{d}})$,

$$\sigma^{*2}(r_{\mathrm{d}}) = \frac{(1/N)\sum_{k=1}^{N}\sigma_k^2(r_{\mathrm{d}})}{\sigma_x^2}. \tag{3.4}$$

Considering a variance measurement valid, too few points for computing a sample variance yields unreliable estimates of the true variance. Jianjun *et al*. [42] suggest that the set of $\Omega_k(r_{\mathrm{d}})$ should contain at least $N_0 = 30$ DVs. A sample of 30 data points for estimating mean or variance is the general rule of thumb [33,36,38,54].

If the two DVs of a predictable signal are close to one another in terms of their Euclidean distance, they should have similar targets. Hence, the presence of a strong deterministic component within a signal will result in smaller target variances for small spans r_{d} [38,42]. The minimal target variance $\sigma_{\min}^{*2} = \min_{r_{\mathrm{d}}}[\sigma^{*2}(r_{\mathrm{d}})]$ represents the amount of uncertainty present within the time series (the prevalence of the stochastic component) and has an upper bound of unity. The reason for this is that all DVs belong to the same set of $\Omega_k(r_{\mathrm{d}})$ when r_{d} is sufficiently large. As a result of the standardization of the distance axes, the resulting DVV plots are relatively easy to interpret. The resulting DVV curves are plotted with the standardized distance r_{d} on the horizontal axis and the normalized variance σ^{*2} on the vertical axis. At the extreme right, DVV plots smoothly converge to unity, because for maximum spans all DVs belong to the same set, and the variance of the targets is equal to the variance of the time series. If this is not the case, the span parameter *nd* should be increased [35,36]. If the surrogate time series yields DVV plots similar to that of original time series, it indicates that the time series is likely to be linear and vice versa [37].

Performing DVV analysis on the original and a number of surrogate time series, a DVV scatter diagram can be produced that characterizes the linear or nonlinear nature of time series using the optimal embedding dimension of the original time series. If the surrogate time series yields DVV plots similar to the original time series, in which case the DVV scatter diagram coincides with the bisector line, then the original time series is adjudged to be linear [35]. Thus, the deviation from the bisector line is an indicator of nonlinearity of the original time series [35,38]. As the degree of signal nonlinearity increases, the deviation from the bisector line grows. The deviation from the bisector line can be quantified by the RMSE between the σ^{*2} values of the original time series and the σ^{*2} values averaged over the DVV plots of the surrogate time series. Thus, a single test statistic t^{DVV} is calculated [36]

$$t^{\mathrm{DVV}} = \sqrt{\left\langle \left(\sigma^{*2}(r_{\mathrm{d}}) - \frac{\sum_{i=1}^{N_s}\sigma_{s,i}^{*2}(r_{\mathrm{d}})}{N_s} \right)^2 \right\rangle_{\mathrm{valid}_{r_{\mathrm{d}}}}}, \tag{3.5}$$

where $\sigma_{s,i}^{*2}(r_{\mathrm{d}})$ is the target variance at the span r_{d} for the ith surrogate, and the average is taken over all spans r_{d} that are valid in all surrogate and original DVV plots.

(b) Discussion on parameters for delay vector variance analysis

For a correct choice of embedding parameters, which might not be unique, the target variance, σ^{*2}, gives information related to its predictability. It is important to determine the embedding dimension and time lag correctly as, in combination with the structured signal, similar delay vectors in terms of their Euclidian distance have similar targets. The embedding dimension m determines how many previous time samples are used for examining the local predictability. It is important to choose m sufficiently large, so that the m-dimensional phase space enables a proper representation of the dynamic system. We used and compared three different approaches when adopting the embedding dimension and time lag. They are presented here for completeness.

The first approach determines the optimal embedding parameters of the signal using a differential entropy method proposed by Mandic *et al*. [37]. The optimal m and time lag, τ, are simultaneously determined based on the estimates of the differential entropy ratio (ER) [55] of the phase-space representation of a sampled time signal and an ensemble of its surrogates. If the temporal span of $(m \cdot \tau)$ is too small, the signal variation within the delay vector is mostly governed by noise and either m or τ should be increased. The set of optimal parameters, $\{m_{\mathrm{opt}}, \tau_{\mathrm{opt}}\}$, yields a phase-space representation which best reflects the dynamics of the underlying signal production system and it is expected that this representation has a minimal differential entropy. The minimum of the plot of the entropy ratio yields the optimal set of embedding parameters. In order to determine the optimum embedding parameters in all simulations $N_{\mathrm{s}} = 5$ surrogates were generated and the entropy ratios were evaluated for $m = 2, 3, \ldots, 10$ and $\tau = 1, 2, \ldots, 10$. Increasing the number of surrogates does not affect results. The ER criterion requires a time series to display a clear structure in phase space; i.e. for signals with no clear structure, the method will not generate a clear minimum, and a different approach needs to be adopted. In practice, it is common to have fixed time lag (sampling rate) and to adjust the embedding dimension (length of filter) accordingly.

The second approach determines the optimal embedding dimension by running a number of DVV analyses for different values of m, and choosing the one for which the minimal target variance, $\sigma^{*2}_{\mathrm{min}}$, is the lowest, i.e which yields the best predictability [33]. In this work, the analysis is performed for embedding dimensions ranging from 2 to 25. The time lag, τ, for convenience, is set to unity in all simulations. This choice of τ is conservative in the context of signal nonlinearity estimation. Assuming the embedding dimension is sufficiently high, a linear time series can be accurately represented using $\tau = 1$, while this is not the case for a nonlinear signal, for which τ plays an important role in its characterization. Hence, if the null hypothesis of linearity is rejected, one can assume that the time series is nonlinear. As the linear part was accurately described for τ equal to unity, the rejection can be attributed to the nonlinear part of the signal. On the other hand, if the null hypothesis is found to hold, the signal is genuinely linear or the phase space is poorly reconstructed using $\tau = 1$, i.e. the signal is actually nonlinear [33].

In the third approach, within the context of nonlinearity detection, m is not considered critical and the optimal embedding dimension of the original time series can be set manually. Gautama *et al*. [35] report relative insensitivity of the DVV method to the parameter choice, which makes this method robust. The time lag is set to unity for convenience. This convenience does not influence the generality of the results to the extent considered in this paper.

The maximal span parameter, n_{d}, determines the range of standardized distances to consider, i.e. controlling the span over which to perform the DVV analysis. Visual inspection of the convergence of the DVV plot to unity should be used for setting this parameter, i.e. typically starting at value $n_d = 2$ and increasing it using unit steps until DVV plots converge to unity. We adopt $n_{\mathrm{d}} = 2$ in all simulations in this paper. The number of standardized distances for which target variances are computed, N_{tv}, has been set to 50. The number of reference DVs considered, N_{sub}, is 200 for all simulations [33,35]. Reducing the size of the subset of DVs to which pairwise Euclidean distances are computed significantly speeds up DVV analysis. For each of the time

series, we perform a set of DVV-based nonlinearity analyses for a range of parameter values using a set of $N_s = 25$ surrogates. Gautama *et al*. [56] have analysed the sensitivity of the proposed DVV method to parameter settings for four different time series, of which three were nonlinear. They found that the embedding dimension, m, and the maximal span, n_d, were the only parameters with a noticeable effect with respect to nonlinearity detection. They also concluded that the effects were minor for reasonable parameter values, i.e. $m \in [3, 10]$ and $n_d \geq 1$.

The authors have carried out prior tests over a number of LDV and load cell experimental studies to ensure that the parameter values chosen for m and τ elicit consistent results that converge to the estimated nonlinearity based on a jointly optimized set of values for these parameters corresponding to the true embedding dimension. For the analysis of the load cell recorded signals, it was found that the first and second approaches are more appropriate, as the DVV plots of measured data and their surrogates converge to unity in most of the cases. Moreover, by comparing the results of DVV analysis of the load cell readings, using these two approaches, it was found that the RMSE varies negligibly between them. In this paper, the results obtained by using the second approach are presented and discussed. For the measurements of displacement and velocity obtained by LDV, the third approach is adopted. It is observed that the recorded data are long (over 25 000 data per measurement) and, because of this, demand long computational times when applying the first and second approach. The first approach was observed to be time consuming and unreliable for large sets of data. The attempt to find the optimal embedding parameter using the first approach was done by segmenting the response signal. The embedding parameters obtained give different values of RMSE of the response signal for the segmented section than the whole signal. RMSE changes using the first approach are representative of changes within the signal but cannot be used to compare two or more different responses of the system with consistent interpretation. It is hard to observe the time-series structure in phase space as a whole, and therefore it is impossible to determine its clear minimum in order to find adequate parameters, m and τ, to represent the response signal. A similar situation is created for the second approach, where the long set of response data takes too long to be processed and the values of the embedding parameter obtained are in most cases out of reasonable range, $m \in [3, 10]$. In order to get consistently comparable results and to speed up data processing, the third approach is adopted where m was set to 3 while τ is equal to unity. The deviation from the bisector line of the scatter plot quantified by RMSE [33] can summarize the result of DVV analysis.

4. Discussion and results

(a) Laser Doppler vibrometer measurements

The LDV has been successfully employed for a wide range of applications, including lifting of roof tiles in a wind tunnel test [57], vibration mode estimation [50,52], estimation of acoustic parameters [51], non-destructive diagnostics of fresco paintings [58], estimation of natural frequencies [59] and damage detection [60]. The fundamental governing principle of the LDV is the Doppler effect. A Polytec RSV-150 remote-sensing vibrometer was used to record the dynamic responses of the TLP model. The TLP model was exposed to sine wave scaled heights of 40, 60 and 90 mm of varying wave periods, as well as two-dimensional Bretschneider, Pierson–Moskowitz and JONSWAP wave spectra, with wave height 60 mm (table 2). Measurements of the displacement and velocity at the base of the central column (figure 1*a* marked with 1) and at the half height of the mast (figure 1*a* marked with 2) were recorded and analysed using the DVV method. The results of the DVV analysis are given in the form of RMSE value using the DVV method for each response measured, which is a measure of the degree of nonlinearity of the measured signal [33,44]. The results of the RMSE of displacement and velocity are shown in figure 2. Detailed results of analyses for LDV-based measurements are presented in the electronic supplementary material (see appendices S1 and S2 for measurements at the mast base and at mid-height, respectively).

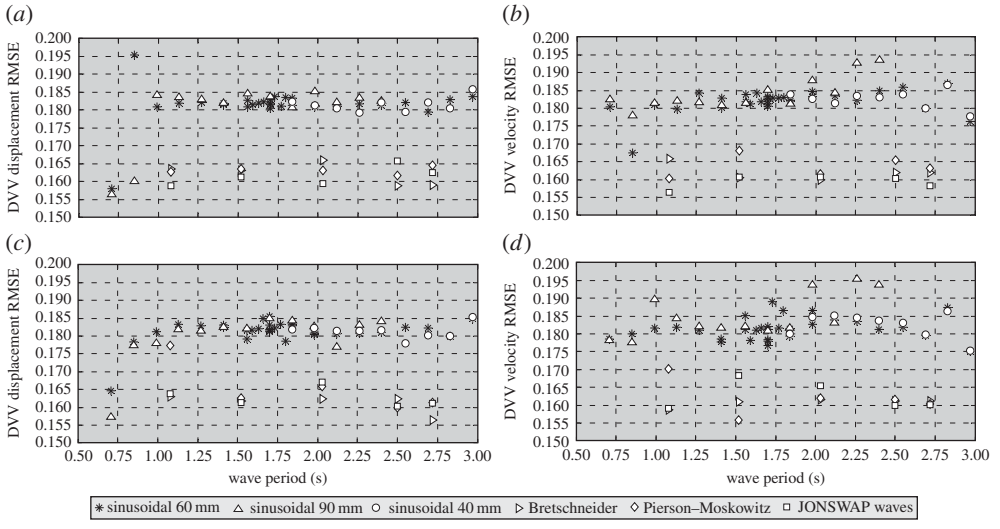

Figure 2. LDV measurements of DVV results versus wave period for: (*a*) mast base displacement; (*b*) mast base velocity; (*c*) mast mid-height displacement; and (*d*) mast mid-height velocity when a TLP is exposed to sine waves with scaled wave height 40, 60 and 90 mm and Bretschneider, Pierson–Moskowitz and JONSWAP wave spectra.

There is a visible trend in the RMSE of the system response signal regardless of the LDV focus point for the wave periods greater than 1.0 s. The results show that the degree of nonlinearity in the system response signal (i.e. displacement and velocity) is greater for the sine wave, regardless of the wave height, than for Bretschneider, Pierson–Moskowitz and JONSWAP wave spectra with 60 mm wave height. For the system excited with sine waves, the RMSE for displacement varies between 0.179 and 0.186 and between 0.177 and 0.186, at measuring point 1 and 2, respectively, excluding less than 1.0 s wave period results. Even though the RMSE results of displacement vary within the similar band for two LDV targeting locations, closer comparison of figure 2*a* and figure 2*c* shows that the plots of RMSE of responses to the sine waves are more scattered for measuring point 2 results within the observed band. For the system excited with sine waves, the RMSE for velocity varies between 0.176 and 0.194 and between 0.175 and 0.195, at measuring point 1 and 2, respectively, excluding less than 1.0 s wave period results. Here, as for the results for displacement, the degree of nonlinearity for the two measuring locations varies within the same range (figure 2*b* and figure 2*d*) and the plots of the RMSE results are more scattered for velocity measured at point 2. The results of DVV analysis of the system response to the Bretschneider, Pierson–Moskowitz and JONSWAP spectra, with 60 mm wave height, show that the degree of nonlinearity of the displacement varies between 0.159 and 0.166 and between 0.156 and 0.167 at measuring point 1 and 2, respectively (figure 2*a*,*c*). The RMSE for velocity of the system, when exposed to Bretschneider, Pierson–Moskowitz and JONSWAP spectra, varies between 0.156 and 0.168 and between 0.156 to 1.170 at measuring point 1 and 2, respectively (figure 2*b*,*d*). However, for Bretschneider, Pierson–Moskowitz and JONSWAP wave spectra only five wave periods are observed. Therefore, it is hard to see the relation between nonlinearities of displacement and velocity, and to compare the results from the two measuring points. Therefore, linear fitting is applied in order to study the potential trend of the degree of nonlinearity for each type of wave excitation. The coefficients for the best linear fitting curves for each load applied and at two observation points are summarized in table 3. Linear fitting for sine wave results shows that there is an increasing trend in displacement and velocity RMSE for sine waves with 60 and 90 mm wave height, while the results for the 40 mm wave height sine wave are inconclusive. The linear fit for Pierson–Moskowitz and JONSWAP spectra shows that displacement and velocity RMSE increases for observation point 1 and decreases for observation point 2, while the results for Bretschneider are inconclusive.

Table 3. Linear basic fitting coefficients obtained for DVV results of LDV measurements versus wave period.

linear fitting $y = a \times x + b$	sine wave 40 mm	sine wave 60 mm	sine wave 90 mm	Bretschneider	Pierson–Moskowitz	JONSWAP
displacement (1)	$a = 0.0018$	$a = 0.0016$	$a = 0.01$	$a = -0.003$	$a = 0.00026$	$a = 0.0029$
	$b = 0.18$	$b = 0.18$	$b = 0.16$	$b = 0.17$	$b = 0.16$	$b = 0.16$
velocity (1)	$a = -0.00174$	$a = 0.0022$	$a = 0.0067$	$a = -0.0016$	$a = 0.00073$	$a = 0.00092$
	$b = 0.187$	$b = 0.18$	$b = 0.17$	$b = 0.17$	$b = 0.16$	$b = 0.16$
displacement (2)	$a = 5.05 \times 10^{-005}$	$a = 0.0024$	$a = 0.0076$	$a = -0.0026$	$a = -0.0083$	$a = -0.0013$
	$b = 0.181$	$b = 0.18$	$b = 0.17$	$b = 0.17$	$b = 0.18$	$b = 0.1$
velocity (2)	$a = -0.003$	$a = 0.00085$	$a = 0.0071$	$a = 0.0012$	$a = -0.0032$	$a = -0.0013$
	$b = 0.19$	$b = 0.18$	$b = 0.17$	$b = 0.16$	$b = 0.17$	$b = 0.17$

(b) Load cell measurements

The TLP was excited by waves of a single frequency for about 1 min in each test. During this time, the responses of the various load cells reached stable and repeated peaks over time. The responses of each load cell owing to the wave conditions listed in table 2 are analysed using the DVV method in order to study the degree of nonlinearity of the recorded signal with the aim of characterizing the behaviour of the system using this marker. The DVV results of the load cell measurement analysis for different wave heights are shown in figure 3. The RMSE values gravitate to the unique value 0.172 for all load cells when wave height is 40 mm (figure 3*a*). In this case, the white load cell measurements show the greatest degree of nonlinearity in the signal ($\mathrm{RMSE}_{\max} = 0.23$) and at the same time the greatest oscillation in the degree of nonlinearity ($\Delta = 0.108$). At closer examination, similar behaviour is observed for the red load cell. The reason is likely to be related to the fact that both these cells are located at the bow position and are in contact with the wave before the other cells. The results for wave height 60 mm also gravitate to a unique value of 0.195 (figure 3*b*). The plot shows that the results are more scattered for the wave periods lower than 2.0 s, while for wave periods greater than 2.0 s the degree of nonlinearity of the records is almost the same. For wave height of 90 mm, the plot of the RMSE for all load cells is even more scattered (figure 3*c*). The averaged RMSE is 0.226 for this case. Hence, it appears that the average RMSE increases with wave height. However, when the wave height is increased to 120 mm the average RMSE is 0.208 (figure 3*d*), which is less than when the height is 90 mm. Still, the plot of RMSE for wave height 120 mm remains scattered. In order to examine the possible correlation between the particular load cell location and wave height, linear basic fitting was applied to the RMSE results shown in figure 3. The coefficients obtained are listed in table 4.

For wave height 40 mm the blue, brown, white and yellow load cells have a negative slope linear fitting function (i.e. the degree of nonlinearity decreases with wave period increase), while the red and green load cells have a positive slope fitting function (i.e. the degree of nonlinearity increases with wave period increase). The white load cell shows the greatest degree of nonlinearity decrease with wave height increase. For the wave height 60 mm, all the load cells, apart from yellow, have a negative slope of linear fitting function. Port load cells, white, blue and brown, show a steeper decrease of nonlinearity for increases in wave period than the starboard load cells, red and green. For the wave height of 90 mm, all load cells experience the decrease of nonlinearity of the measurements for increases in wave period. In this case, the decrease in the response nonlinearity is the greatest for the port load cells, brown and white. Finally, for the wave height 120 mm, the red and white load cells have positive slope, indicating an increase in the nonlinearity of the response with the increase of the wave period. All the other load cells have negative slopes, where again the brown load cell measurement shows the greatest decrease in

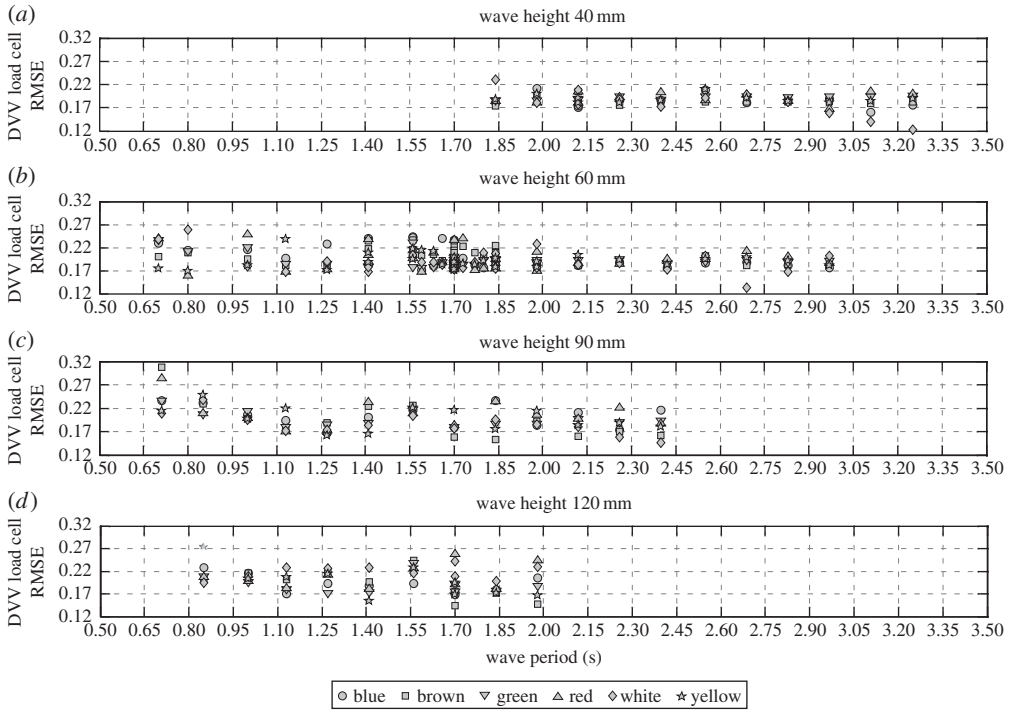

Figure 3. Load cells DVV results versus wave period for scaled wave height: (*a*) 40 mm; (*b*) 60 mm; (*c*) 90 mm; and (*d*) 120 mm.

Table 4. Linear basic fitting coefficients obtained for DVV results of load cell measurements versus wave period.

$y = a \times x + b$		blue—amidships port	brown—stern port	green—stern starboard	red—bow starboard	white—bow port	yellow—amidships starboard
40 mm	*a*	−0.0084	−0.0047	0.0074	0.0040	−0.0500	−0.0031
	b	0.21	0.20	0.17	0.18	0.30	0.20
60 mm	*a*	−0.0220	−0.0110	−0.0089	−0.0054	−0.0160	0.0009
	b	0.24	0.22	0.21	0.20	0.22	0.19
90 mm	*a*	−0.0120	−0.0550	−0.0160	−0.0140	−0.0300	−0.0190
	b	0.22	0.28	0.22	0.23	0.23	0.23
120 mm	*a*	−0.0260	−0.0520	−0.0084	0.0250	0.0120	−0.0650
	b	0.23	0.27	0.20	0.17	0.20	0.29

nonlinearity degree. All the above indicates that there is a relationship between the load cell performance and the wave period. The next step is to examine the relationship between the degree of nonlinearity of the load cell measurements and the wave height (figure 4).

Figure 4 shows the results of DVV analysis of the load cell measurements for different wave heights observed for each load cell separately. It appears that the plots are scattered and there is no correlation between the wave heights and the degree of linearity. The results for the bow cells show that the difference between the greatest and the lowest nonlinearity observed is 0.136 and 0.125, for white and red, respectively. The difference in RMSE extremes for amidships load cells is lower, i.e. 0.083 and 0.120 for blue and yellow, respectively, and the plots appear to be less scattered than for the bow load cells. The differences in the RMSE of the stern load cells are

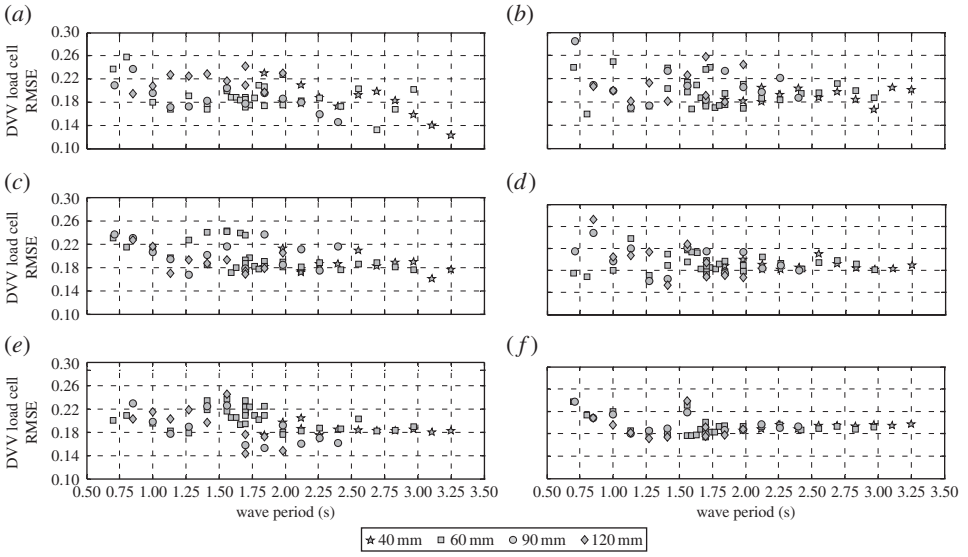

Figure 4. Load cell DVV results versus wave period for 40, 60, 90 and 120 mm. Scaled wave heights: (*a*) white—bow Port; (*b*) red—bow starboard; (*c*) blue—amidships port; (*d*) yellow—amidships starboard; (*e*) brown—stern port; and (*f*) green—stern starboard.

0.101 and 0.068, for brown and green, respectively, and the plots appear to converge to the unique value 0.2 with the increase in wave period. Furthermore, closer observation of figure 4 shows that for the wave periods greater than 2.00 s all the plots show that the RMSE varies around the same value regardless of the wave height. The band of the RMSE variation is wider for the bow load cells as they are first to be 'hit' by the waves while the steel gravity anchorage base that they are attached to resists the pitch motions. A detailed summary of results is provided in the electronic supplementary material, appendix S3.

The DVV method is also investigated to test its robustness against noise present with an underlying signal. In that regard, the results of DVV analysis of sinusoidal waves with different periods (T, $2T$, $4T$, $8T$, $16T$ and $32T$) and varying level of noise (0, 0.5, 1, 5, 10, 15, 20, 25, 50, 75 and 100%) are tested. The variation in RMSE for the low level of noise, from no noise to 15% noise, is small regardless of the wave period observed. This indicates that the DVV method is robust for low to medium levels of noise within the signal. For higher levels of noise the trend changes. Hence, for longer wave periods (T, $2T$, $4T$ and $8T$), the increase in nonlinearity of the signal is noticeable for noise exceeding 50%. For the shorter period waves, the RMSE trend changes from noise level 25%. In general, the highest change in RMSE for all observed cases is for 75% and 100% noise. A graph of these RMSE values against various noise levels is presented in the electronic supplementary material, appendix S4.

5. Conclusion

This paper has employed the DVV method for the estimation, assessment and interpretation of signal nonlinearities of detailed testing of a TLP wind turbine support structure in an ocean wave basin, from output-only conditions. The regular waves of varying height, along with the Bretschneider, the Pierson–Moskowitz and the JONSWAP spectra of realistic sea states, have been used as an input to this structure. The dynamic responses in the form of displacement and velocity as well as the tension force of the structure have been measured at different locations using a LDV and load cells, respectively. The degrees of nonlinearity of the recorded responses of the system are obtained for various wave heights using DVV methodology.

Analysis of the LDV measurements shows segregation of the RMSE for sine waves of different heights on one side and the Bretschneider, the Pierson–Moskowitz and the JONSWAP spectra on the other side. The degree of estimated signal nonlinearity observed is approximately 0.182 for regular waves and 0.162 for different sea spectra used in the study, regardless of the type of the response of the system and the location of LDV focus point observed. It is shown that the results are insensitive to the change in wave height. However, it is observed that the velocity RMSE plots are more scattered than the RMSE obtained for displacement. Also, the RMSE values appear to be more scattered when the LDV focus point is at the half-way point on the mast than at the base. These results indicate that by analysis of the nonlinearity of the signal responses it is possible to access the type of excitation force and the location of the measurements. Moreover, the results can be used to monitor the consistency of measurement devices used for monitoring.

Analysis of the load cell measurements shows that there is no obvious trend in the nonlinearity for different wave heights. However, the plots of RMSE show that for the low heights of the waves the results of all load cells gravitate to a unique value, while the graph becomes more scattered for higher wave heights. There seems to be a relationship between the load cell locations and the incident wave direction when the DVV results are compared. The load cells at the bow have a higher variation in the degree of nonlinearity as the tension force increases due to system resistance to pitch motions. A similar trend, but with lower variation in the degree of nonlinearity, is observed for load cells located at amidships. This is in agreement with the findings of Lynch & Murphy [61] that for the operation of a floating wind turbine pitch and roll motions may affect the tower loads. Additionally, the lowest magnitude of signal nonlinearity computed corresponds to load cells located at the stern. Moreover, for wave periods greater than 2 s the nonlinearities converge to a unique value regardless of the wave height, indicating that the dynamic signature of the device can become consistent beyond a certain wave period and become independent of such wave periods. A comprehensive theoretical study connecting a large number of wind and wave interaction conditions with the TLP would be helpful in the future to understand and quantify the extent to which system nonlinearities may be related to signal nonlinearities. In particular, studies related to ocean engineering phenomena, such as dynamics related to selective excitation of frequencies by second-order difference or sum-frequency wave diffraction forces, may be interesting.

Scaled model testing of a TLP supporting a wind turbine, in conjunction with appropriate statistical markers for monitoring dynamic responses, is observed to be helpful for benchmarking the dynamic responses and has the potential to better inform engineers in selecting monitoring, identification or control strategies even at the design stage. This paper also indicates that the methodology presented is scalable to larger models or full-scale structures. There is only some qualitative interpretation or information regarding the input loadings that are required to carry out the analysis and in principle the method can work from a perfectly output-only perspective as well. Access is a key issue once the platforms are installed and, consequently, the presented methodology is very helpful as measuring inputs to the system can be very difficult under high wind and wave conditions. On the other hand, it is relatively easier to obtain the dynamic responses of the structure as an output. When the structures are still at a test level or model level, the method can identify aspects related to monitoring using estimated signal nonlinearity quantification. These advantages of the method directly help to lower certain costs. Specifically, the cost of installation can be avoided by possibly removing the requirement of installing high-precision sensors measuring exposure to wind and wave in detail when indicators based only on outputs are helpful. Long-distance monitoring can avoid the requirement of access and also improves the safety of people who typically access the sites of these structures under calm conditions, often characterized by ‘weather windows’. Approaches related to use of output-only conditions in conjunction with statistical markers, similar to the approach presented in this paper, may significantly lower the cost of access and probably the insurance as well. The approach can also be important as a marker for changing structural conditions when a device is being monitored. Finally, the scalable aspect of the methodology avoids the cost of having to repeatedly demonstrate the method at different model scales.

Acknowledgements. The authors express their gratitude to Joe Armstrong of Polytec for providing the researchers with the Polytec RSV 150 laser Doppler vibrometer used in the experiments reported in this paper. The authors also express their gratitude to Keith O'Sullivan, Hydraulics and Maritime Research Centre, for his technical support in relation to the test set-up.

Funding statement. The authors acknowledge Marine Research Energy Ireland (MaREI), grant no. 12/RC/2302, a Science Foundation Ireland (SFI) supported project and SFI Advance award 14/ADV/RC3022.

References

1. Jeffrey H, Sedgwick J. 2011 *ORECCA European offshore renewable energy roadmap*. Edinburgh, UK: ORECCA Coordinated Action Project.
2. Arapogianni A *et al*. 2007 *Deep water—the next step for offshore wind energy*. Brussels, Belgium: The European Wind Energy Association (EWEA).
3. Beaudry-Losique J *et al*. 2011 *A national offshore wind strategy: creating an offshore wind energy industry in the United States*. US Department of Energy, Office of Energy Efficiency and Renewable Energy, Wind & Water Power Program; US Department of the Interior, Bureau of Ocean Energy Management, Regulation, and Enforcement. See http://www1.eere.energy.gov/wind/pdfs/national_offshore_wind_strategy.pdf.
4. Carbontrust. 2012 *Technology innovation needs assessment* (*TINA*): *offshore wind power summary report*. Low Carbon Innovation Coordination Group. See https://www.gov.uk/government/uploads/system/uploads/attachment_data/file/48279/4467-tina-offshore-wind-summary.pdf.
5. Bulder BH, Henderson A, Huijsmans RHM, Peeringa JM, Pierik JTG, Snijders EJB, van Hees MT, Wijnants GH, Wolf MJ. 2003 Floating offshore wind turbines for shallow waters. In *Proc. European Wind Energy Association* (*EWEC 2003*), *Madrid, Spain, 16–19 June 2003*. Brussels, Belgium: EWEA.
6. Godø SN. 2013 *Dynamic response of floating wind turbines*. Trondheim, Norway: Department of Marine Technology, Norwegian University of Science and Technology.
7. Andrus C. 2011 Floating foundation for offshore wind turbines. *Ship Offshore* **3**, 58–59.
8. INWORK. 2013 *Floating offshore wind foundations: industry consortia and projects in the United States, Europe and Japan. An overview*. Main(e) International Consulting LLC. See http://www.compositesworld.com/cdn/cms/uploadedFiles/floating_offshore_wind_consortia.pdf.
9. Ishihara T, Taki S. 2014 *Fukushima offshore wind consortium: Fukushima floating offshore wind farm demonstration project* (*Fukushima FORWARD*). Tokyo, Japan: Department of Civil Engineering School of Engineering, University of Tokyo.
10. PrinciplePower. 2009–2011 *WindFloat*. See http://www.principlepowerinc.com/products/windfloat.html.
11. Butterfield S, Musial W, Jonkman J, Sclavounos P, Wayman L. 2005 Engineering challenges for floating offshore wind turbines. In *Proc. Copenhagen Offshore Wind Conf.* (*COW05*), *Copenhagen, Denmark, 26–28 October 2005*. Brussels, Belgium: EWEA.
12. Jonkman JM. 2007 *Dynamics modeling and loads analysis of an offshore floating wind turbine*. Technical Report NREL/TP-500–41958. National Renewable Energy Laboratory. See http://www.nrel.gov/docs/fy08osti/41958.pdf.
13. Breton S-P, Moe G. 2009 Status, plans and technologies for offshore wind turbines in Europe and North America. *Renew. Energy* **34**, 646–654. (doi:10.1016/j.renene.2008.05.040)
14. Manuel L, Sweetman B, Winterstein SR. 2001 Analytical predictions of the air gap response of floating structures. *J. Offshore Mech. Arct. Eng.* **123**, 112–117. (doi:10.1115/1.1372195)
15. Winterstein SR, Sweetman B. 2001 Air gap response of floating structures: statistical predictions versus observed behavior. *J. Offshore Mech. Arct. Eng.* **123**, 118–123. (doi:10.1115/1.1377867)
16. Nielsen FG, Hanson TD, Skaare B. 2006 Integrated dynamic analysis of floating offshore wind turbines. In *Proc. OMAE 2006, Hamburg, Germany, 4–9 June 2006*. New York, NY: ASME.
17. Agarwal P, Manuel L. 2009 Simulation of offshore wind turbine response for long-term extreme load prediction. *Eng. Struct.* **31**, 2236–2246. (doi:10.1016/j.engstruct.2009.04.002)
18. Han SM, Benaroya H. 2002 Comparison of linear and nonlinear responses of a compliant tower to random wave forces. *Chaos Solitons Fractals* **14**, 269–291. (doi:10.1016/S0960-0779(01)00232-6)
19. Islam N, Zaheer MM, Ahmed S. 2009 Double hinged articulated tower interaction with wind and waves. *J. Wind Eng. Ind. Aerodyn.* **97**, 287–297. (doi:10.1016/j.jweia.2009.07.002).

20. Waris MB, Ishihara T. 2012 Dynamic response analysis of floating offshore wind turbine with different types of heave plates and mooring systems by using a fully nonlinear model. *Coupled Syst. Mech.* **1**, 247–268. (doi:10.12989/csm.2012.1.3.247)
21. Murphy J, O'Shea R, O'Sullivan K, Pakrashi V. 2013 Dynamic responses of a scaled tension leg platform, wind turbine support structure in a wave tank. *Key Eng. Mater.* **569–570**, 563. (doi:10.4028/www.scientific.net/KEM.569-570.563)
22. DET NORSKE VERITAS. 2013 *Design of floating wind turbine structures*. Offshore Standard DNV-OS-J103. See http://www.dnv.com.
23. Federal Maritime and Hydrographic Agency (BSH). 2007 *Standard: design of offshore wind turbines*. BSH no. 7005. See http://www.onlinepubs.trb.org/onlinepubs/mb/Offshore%20Wind/Standard.pdf.
24. Pakrashi V, O'Sullivan K, O'Shea R, Murphy J. 2013 Experimental responses of a monopile foundation with a wave energy converter attached. In *Proc. Hydro 2013 International, Chennai, India, 4–6 December 2013*. Chennai, India: Indian Institute of Technology Madras.
25. Swartz RA, Lynch JP, Zerbst S, Sweetman B, Rolfes R. 2010 Structural monitoring of wind turbines using wireless sensor networks. *Smart Struct. Syst.* **6**, 183–196.
26. Bian C, Ning X. 2004 Evaluating age-related loss of nonlinearity degree in short-term heartbeat series by optimum modeling dimension. *Physica A* **337**, 149–156. (doi:10.1016/j.physa.2004.01.040)
27. Tsonis AA, Heller FL, Tsonis PA. 2002 Probing the linearity and nonlinearity in DNA sequences. *Physica A* **312**, 458–468. (doi:10.1016/S0378-4371(02)00859-2)
28. Su Z-Y, Wu T, Yang P-H, Wang Y-T. 2008 Dynamic analysis of heartbeat rate signals of epileptics using multidimensional phase space reconstruction approach. *Physica A* **387**, 2293–2305. (doi:10.1016/j.physa.2007.12.008)
29. Schreiber T, Schmitz A. 2000 Surrogate time series. *Physica D* **142**, 346–382. (doi:10.1016/s0167-2789(00)00043-9)
30. Theiler J, Eubank S, Longtin A, Galdrikian B, Doyne Farmer J. 1992 Testing for nonlinearity in time series: the method of surrogate data. *Physica D* **58**, 77–94. (doi:10.1016/0167-2789(92)90102-S)
31. Schreiber T, Schmitz A. 1996 Improved surrogate data for nonlinearity tests. *Phys. Rev. Lett.* **77**, 635–638. (doi:10.1103/PhysRevLett.77.635)
32. Hegger R, Kantz H, Schreiber T. 1999 Practical implementation of nonlinear time series methods: the TISEAN package. *Chaos* **9**, 413–433. (doi:10.1063/1.166424)
33. Gautama T, Mandic DP, Hulle MMV. 2003 Signal nonlinearity in fMRI: a comparison between BOLD and MION. *IEEE Trans. Med. Imagining* **22**, 636–644.
34. Mandic DP, Chambers JA. 2001 Some practical considerations of predictability and learning algorithms for various signals. In *Recurrent neural networks for prediction: learning algorithms, architectures and stability* (ed. S Haykin), pp. 171–198. Chichester, UK: John Wiley & Sons Ltd.
35. Gautama T, Mandic DP, Hulle MMV. 2004 The delay vector variance method for detecting determinism and nonlinearity in time series. *Physica D* **190**, 167–176. (doi:10.1016/j.physd.2003.11.001)
36. Gautama T, Mandic DP, Hulle MMV. 2003 Indications of nonlinear structures in brain electrical activity. *Phys. Rev. E* **67**, 046204(5). (doi:10.1103/PhysRevE.67.046204)
37. Mandic DP, Chen M, Gautama T, Van Hulle MM, Constantinides A. 2008 On the characterization of the deterministic/stochastic and linear/nonlinear nature of time series. *Proc. R. Soc. A* **464**, 1141–1160. (doi:10.1098/rspa.2007.0154)
38. Gautama T, Hulle MMV, Mandic DP. 2004 *On the characterisation of the deterministic/stochastic and linear/nonlinear nature of time series*. DPM-04–05. London, UK: Imperial College London.
39. Kuntamalla S, Reddy RGL. 2011 The effect of aging on nonlinearity and stochastic nature of heart rate variability signal computed using delay vector variance method. *Int. J. Comput. Appl.* **14**, 40–44. (doi:10.5120/1837-2470)
40. Addo PM, Billo M, Guegan D. 2012 Understanding exchange rates dynamics. In *Proc. 20th Int. Conf. on Computational Statistics* (*COMPSTAT 2012*), *Limassol, Cyprus, 27–31 August 2012*. The Hague, The Netherlands: International Statistical Institute.
41. Schreiber T. 1999 Interdisciplinary application of nonlinear time series methods. *Phys. Rep.* **308**, 1–64.
42. Jianjun Y, Haijun W, Chunming X, Yiqin W, Fufeng L, Rui G, Tiancai M. 2008 Nonlinear analysis in TCM acoustic diagnosis using delay vector variance. In *Proc. 2nd Int. Conf.*

on Bioinformatics and Biomedical Engineering (*ICBBE 2008*), *Shanghai, China, 16–18 May 2008*. Piscataway, NJ:IEEE.
43. Andrzejak RG, Lehnertz K, Mormann F, Rieke C, David P, Elger CE. 2001 Indications of nonlinear deterministic and finite-dimensional structures in time series of brain electrical activity: dependence on recording region and brain state. *Phys. Rev. E* **64**, 061907. (doi:10.1103/PhysRevE.64.061907)
44. Hongying H, Fuliang Y. 2009 Diesel engine fault information acquisition based on delay vector variance method. In *Proc. 2nd Int. Symp. on Knowledge Acquisition and Modeling* (*KAM '09*), *Wuhan, China, 30 November–1 December 2009*. Piscataway, NJ: IEEE.
45. Casale C, Lembo E, Serri L, Viani S. 2010 Preliminary design of a floating wind turbine support structure and relevant system cost assessment. *Wind Eng.* **34**, 29–50. (doi:10.1260/0309-524X.34.1.29)
46. Sclavounos PD, Lee S, DiPietro J, Potenza G, Caramuscio P, De Michele G. 2010 Floating offshore wind turbines: tension leg platform and taught leg buoy concepts supporting 3–5 MW wind turbines. In *Proc. European Wind Energy Conference* (*EWEC 2010*), *Warsaw, Poland, 20–23 April 2010*. Brussels, Belgium: EWEA.
47. Lefebvre S, Collu M. 2012 Preliminary design of a floating support structure for a 5MW offshore wind turbine. *Ocean Eng.* **40**, 15–26. (doi:10.1016/j.oceaneng.2011.12.009)
48. Jain A, Robertson AN, Jonkman JM, Goupee AJ, Kimball RW, Swift AHP. 2012 FAST code verification of Scaling Laws for DeepCwind floating wind system tests. In *Proc. 22nd Int. Offshore and Polar Engineering Conf., Rhodes, Greece, 17–23 June 2012*. Mountain View, CA: International Society of Offshore and Polar Engineers (ISOPE). See http://www.isope.org/publications/proceedings/ISOPE/ISOPE%202012/start.htm.
49. Robertson AN, Jonkman JM, Masciola MD, Molta P, Goupee AJ, Coulling AJ, Prowell I, Browning J. 2013 Summary of conclusions and recommendations drawn from the deepcwind scaled floating offshore wind system test campaign. In *Proc. ASME 2013 32nd Int. Conf. on Ocean, Offshore and Arctic Engineering, Nantes, France, 9–14 June 2013*. Brussels, Belgium: NREL.
50. Vanlanduit S, Cauberghe B, Guillaume P, Verboven P. 2004 Automatic vibration mode tracking using a scanning laser Doppler vibrometer. *Opt. Lasers Eng.* **42**, 315–326. (doi:10.1016/j.optlaseng.2003.07.001)
51. Vuye C, Vanlanduit S, Guillaume P. 2009 Accurate estimation of normal incidence absorption coefficients with confidence intervals using a scanning laser Doppler vibrometer. *Opt. Lasers Eng.* **47**, 644–650. (doi:10.1016/j.optlaseng.2009.01.003)
52. Siringoringo DM, Fujino Y. 2009 Noncontact operational modal analysis of structural members by laser Doppler vibrometer. *Comput Aided Civil Infrastruct. Eng.* **24**, 249–265. (doi:10.1111/j.1467-8667.2008.00585.x)
53. Dean RG, Dalrymple RA. 1991 *Water wave mechanics for engineers and scientists*. Singapore: World Scientific.
54. ur Rehman N, Mandic DP. 2009 Qualitative analysis of rotational modes within three dimensional empirical mode decomposition. In *Proc. IEEE Int. Conf. on Acoustics, Speech and Signal Processing* (*ICASSP 2009*), *Taipei, Taiwan, 19–24 April 2009*. Piscataway, NJ: IEEE.
55. Beirlant J, Dudewicz EJ, Gyorfi L, Meulen ECVD. 2001 Nonparametric entropy estimation: an overview. *Int. J. Math. Stat. Sci.* **6**, 17–39.
56. Gautama T, Mandic DP, Van Hulle MM. 2003 A differential entropy based method for determining the optimal embedding parameters of a signal. In *Proc. IEEE Int. Conf. on Acoustics, Speech, and Signal Processing*, vol. 6 (*ICASSP '03*), *Hong Kong, 6–10 April 2003*, pp. 29–32. Piscataway, NJ: IEEE.
57. Okamoto S, Nanba R, Shibao K, Satou M, Shibao Y. 2007 Research on vibration and scattering of roof tiles by wind tunnel test. *J. Environ. Eng.* **2**, 237–246. (doi:10.1299/jee.2.237)
58. Castellini P, Paone N, Tomasini EP. 1996 The laser Doppler vibrometer as an instrument for nonintrusive diagnostic of works of art: application to fresco paintings. *Opt. Lasers Eng.* **25**, 227–246. (doi:10.1016/0143-8166(95)00073-9)
59. Senatore A. 2006 Measurement of the natural frequencies of a uniform rod loaded with centrifugal forces using a laser Doppler vibrometer. *Meas. Tech.* **49**, 43–48. (doi:10.1007/s11018-006-0060-5)
60. Khan AZ, Stanbridge AB, Ewins DJ. 2000 Detecting damage in vibrating structures with a scanning LDV. *Opt. Lasers Eng.* **32**, 583–592. (doi:10.1016/S0143-8166(00)00004-X)
61. Lynch K, Murphy J. 2012 *Overview of offshore wind and ocean energy technologies*. Cork, Ireland: Hydraulics and Maritime Research Centre (HMRC), University College Cork.